Experimental Aerodynamic Analysis of a 4.6%-Scale Flying-V Subsonic Transport

Palermo, Marco; Vos, Roelof

DOI
10.2514/6.2020-2228

Publication date
2020

Document Version
Final published version

Published in
AIAA Scitech 2020 Forum

AIAA SciTech Forum
6-10 January 2020, Orlando, FL
AIAA Scitech 2020 Forum

10.2514/6.2020-2228

Experimental Aerodynamic Analysis of a 4.6%-Scale Flying-V Subsonic Transport

Marco Palermo* and Roelof Vos†
Delft University of Technology, Delft, the Netherlands, 2629HS

The experimental investigation into the aerodynamic characteristics of a 4.6%-scale half-model of a flying-wing transport aircraft is detailed. The study is performed in an open-jet wind tunnel where forces and moments are recorded using a 6-axis balance. Two control surfaces in the outboard wing are deflected to measure their effect in terms of lift, drag, and pitching moment up to a Reynolds number of 1 million. The results are subsequently combined with the estimated thrust force using a flight mechanics model of the aircraft in order to predict the most forward and most aft center-of-gravity locations for which the aircraft can be balanced with the control surfaces, while still being statically stable. The results show that the aircraft can attain an untrimmed maximum lift coefficient of 1.02 at an angle of attack of 35 degrees. Furthermore, the pitching moment around the leading-edge of the mean geometric chord is negatively correlated to the angle of attack up to 19 degrees, after which a strong pitch-break is observed, making the aircraft statically unstable. This is associated with a forward shift of the aerodynamic center to a longitudinal position 35%$\bar{c}$ ahead of the moment reference point which is caused by the formation of strong vortices over the wing surface. The effectiveness of the control surfaces hardly deteriorates with angle of attack and all three control surfaces are shown to be effective up to the maximum lift coefficient. Analysis shows that the center-of-gravity location should reside between [-7.5; 0.5] %$\bar{c}$, in power-off conditions, and between [-6; 1] %$\bar{c}$, in power-on conditions, from the leading edge of the mean geometric chord to ensure an ultimate static stability margin of 4.4% as well and a minimum landing speed of 20 m/s. Within these ranges, trimmed maximum lift coefficient values of 0.68 and 0.66 can be achieved respectively in power-off and power-on conditions.

Nomenclature

Latin Symbols

AR	=	aspect ratio (∼)
b	=	reference span (m)
$\bar{c}$	=	mean geometric chord (m)
c	=	chord (m) or constraint (∼)
C_D	=	drag coefficient (∼)
C_L	=	lift coefficient (∼)
C_M	=	pitching moment coefficient (∼)
C_{M_α}	=	pitching moment coeff. derivative $(1/deg)$
C_X	=	force coeff, in x-dir. (∼)
C_Z	=	force coeff, in z-dir. (∼)
g	=	gravitational acceleration (m/s^2)
I	=	interval
l	=	length (m)
L	=	lift force (N)
$\dot{q}$	=	pitch acceleration (deg/s^2)
S	=	surface area (m^2)
$\dot{u}$, $\dot{v}$, $\dot{w}$	=	acceleration in (X, Y, Z)-direction (m/s^2)
V	=	volume (m^3)
x, y, z	=	coord. in body ref. frame (m)

Greek Symbols

α	=	angle of attack (deg)
β	=	side-slip angle (deg)
ξ_{ij}	=	mutual interaction factor (∼)
δ	=	deflection angle (deg)
$\hat{\delta}$	=	control sett. (∼)
Δ	=	deviation of from average (∼)
θ	=	pitch attitude angle (deg)
Λ	=	sweep angle (deg)
γ	=	flight path angle (deg)
ρ	=	density (kg/m^3)
η	=	dimensionless spanwise position (∼)
τ	=	control surface chord ratio (∼)

Subscripts

*Researcher, Faculty of Aerospace Engineering
†Assistant professor, Faculty of Aerospace Engineering, Associate Fellow AIAA.

0	=	zero-lift
A	=	aerodynamic
eq	=	equality
i, j	=	integer
in	=	inboard or inequality
out	=	outboard
max	=	maximum
min	=	minimum
ref	=	reference
T	=	thrust
w	=	wing

Acronyms

AC	=	Aircraft
ac	=	Aerodynamic Center
BWB	=	Blended-Wing-Body
CFD	=	Computational Fluid Dynamics
CoG	=	Center of Gravity
CS	=	Control Surface
CSDR	=	Control Surface Deflection Ratio
KBE	=	Knowledge Based Engineering
LE	=	Leading edge
MGC	=	Mean Geometric Chord
MTOM	=	Max Take-Off Mass
MSS	=	Static Stability Margin
OJF	=	Open Jet Facility
Re	=	Reynolds number
RANS	=	Reynolds Averaged Navier Stokes
SFT	=	Scaled Flight Testing

I. Introduction

The Flying V is a flying-wing transport aircraft, designed to transport 314 passengers in a two-class configuration over a range of 15,000 km. This novel configuration has been conceived at Airbus [1] and has been further developed at Delft University of Technology. It features winglets with rudders for directional stability and control and trailing-edge elevons for pitch and roll control. The wing houses the passenger cabin, the cargo compartment and the fuel tanks, while the engines are mounted above and behind the wing. Its cranked wing has an inboard quarter-chord sweep angle of 63.5 degrees, while the outboard wing has a quarter-chord sweep angle of 34.5 degrees. Combined with an aspect ratio of only 4.7 and the absence of high-lift devices, this requires the aircraft to achieve large angles of attack during the approach phase if a 145 kt speed is to be maintained. This also results in rather long main landing gear legs, as can be seen in Figure 1. An important feature that sets the Flying V apart from any other flying-wing aircraft is the ability to easily stretch and shrink the inboard wing. This allows for a family of aircraft with passenger numbers ranging from 275 to 355 in a standard 2-class configuration.

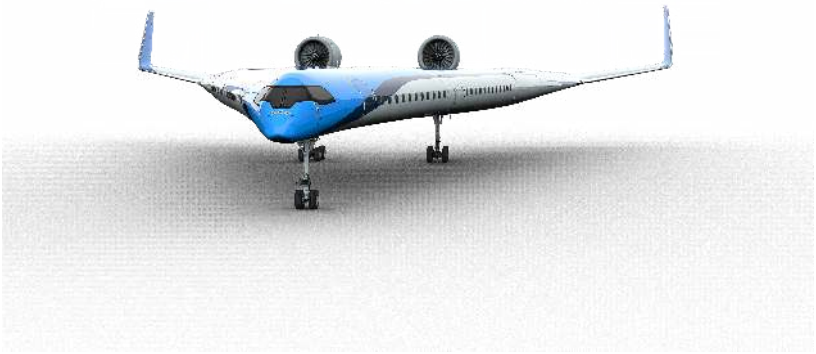

Fig. 1 Conceptual design of a Flying-V aircraft.

The aerodynamic design of this aircraft has been conducted in a previous study [2], considering only the design condition (i.e. Mach number of 0.85 at an altitude of 13km). Based on this study, the Flying V is expected to have a lift-to-drag ratio of at least 23.5 in cruise conditions, confirming the predictions of improved aerodynamic efficiency of flying wings over conventional aircraft evidenced by many authors [3–7]. Other, confidential studies have been conducted in collaboration with Airbus to estimate the structural weight of this aircraft in comparison to a tube-and-wing aircraft designed for the same mission. Based on the results from these studies, it was concluded that the Flying V configuration has the potential to reduce fuel burn over a given, long-range mission by roughly 20%. This warrants

further investigation into this configuration, primarily into its flight characteristics in off-design conditions. Others have achieved this by conducting free-flight experiments of scaled versions of their design [8–10].

To demonstrate adequate handling qualities of the Flying V at low speed, work is under way at Delft University of Technology to build a 4.6%-scale flight demonstrator. Given the high sweep angle and low aspect ratio of the wing, the low-speed aerodynamics of this demonstrator are hard to predict in advance, which hampers a proper assignment of the center-of-gravity location. Particularly at high angles of attack, vortex formation is anticipated, which can dramatically alter the location of the aerodynamic center and therefore the stability margin of the aircraft. Therefore, a low-speed wind-tunnel investigation is conducted on a 4.6% scale half-model of the Flying V in the Open Jet Facility at Delft University of Technology. The goal of this experiment is to measure the change in lift, drag, and pitching moment with angle-of-attack. Furthermore, the pitch control authority is also measured. Based on these measurements, an estimation of the aerodynamic-center location is made. With a trim analysis, this results in a proposed location for the center-of-gravity of the flight demonstrator.

This paper presents the results of the low-speed wind tunnel experiments along with a trim analysis that proposes a center-of-gravity location. The paper is structured as follows. In Sec. II, the experimental setup is described along with a description of the test article. In Sec. III a subset of the experimental results are compared to predictions made by CFD. The differences and similarities are presented and discussed. In Sec. IV, the results of the wind tunnel campaign are presented along with the results of the trim analysis. Finally, in Sec. V, the conclusions are drawn.

II. Methodology

A. Model Description

The Flying V half-model is representative of a 4.6% geometrically scaled Flying V aircraft. The planform view of the half-model is presented in Fig. 2. The chord, leading edge locations, spanwise location and leading edge sweep angles are reported in Table 1 for the four sections that define the outer shape of the wing and for the mean geometric chord section. In Fig. 2, the mean geometric chord, MGC, is also drawn and measures 820mm. The semi-span of the aircraft is 1495mm, while the reference area, $S_{\text{ref}} = 0.9345\text{m}^2$.

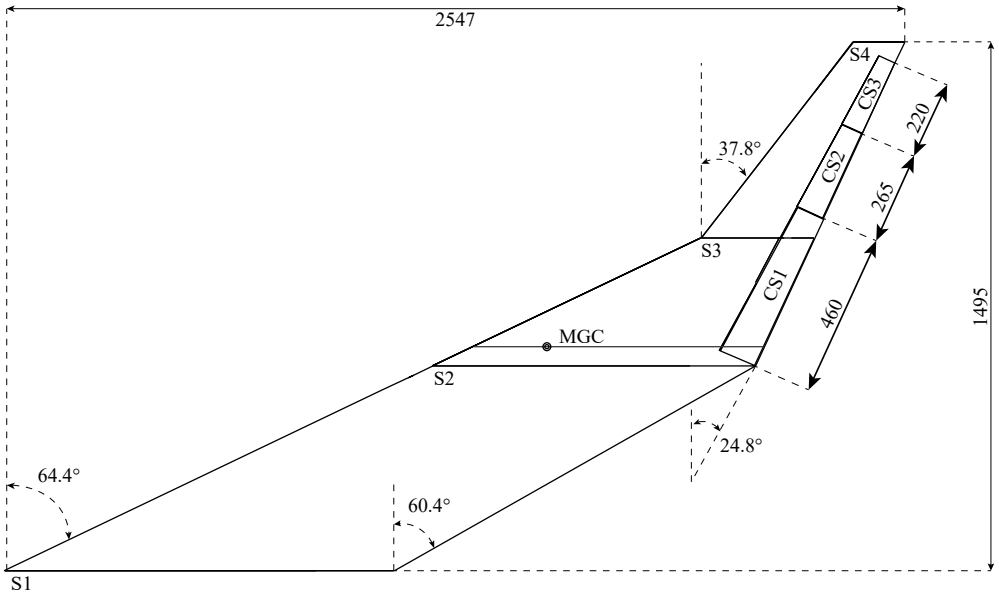

Fig. 2 Flying V model planform top view. Dimensions in mm.

The leading edge sweep is equal to 64.4 degrees up to $\eta \approx 0.63$. At that point, the leading edge sweep angle reduces to 37.8 degrees up to the tip. The outer wing, $\eta \approx [0.63, 1.00]$, features 4.3 degrees of washout at the tip. The model features three independent control surfaces at the trailing edge of the two outer trunks. The local chords, chord ratios, areas, area ratios and volumetric coefficients of the control surfaces reported in Table 2. A positive deflection of a control surface induces the trailing-edge of the control surface to shift downward.

Table 1 Wing planform data.

Section	c	x_{LE}	$x_{1/4c}$	y	η	Λ_{LE}
1	1.104	0.00	0.276	0.00	0.00	64.4
2	0.910	1.215	1.442	0.578	0.38	64.4
3	0.318	1.971	2.050	0.940	0.63	37.8
4	0.145	2.401	2.438	1.495	1.00	37.8
MGC	0.821	1.329	1.534	0.632	0.42	64.4

Table 2 Geometric data of the control surfaces.

CS	c_{in_w}	c_{out_w}	c_{in_cs}	c_{out_cs}	τ_{in}	τ_{out}	$x_{1/4\bar{c}_\text{cs}}$	$y_{1/4\bar{c}_\text{cs}}$	S_cs	S_cs/S_w	V_cs/V_w
1	0.522	0.244	0.109	0.080	0.21	0.33	1.949	0.852	0.158	0.084	0.105
2	0.244	0.183	0.080	0.064	0.33	0.35	2.222	1.178	0.056	0.030	0.057
3	0.183	0.132	0.064	0.050	0.35	0.38	2.360	1.378	0.034	0.018	0.040

B. Experimental Approach

The half model of the Flying V is constructed out of a semi-monocoque structure employing two main spars connected by ribs. Skins, spars and ribs are all made from glass-fibre-reinforced plastic, which is locally stiffened by foam cores. The internal structure is also to be used on a free-flight test article and weighs in total 4.6 kg. Three digital servos are installed inside the wing to remotely control the deflections of the three control surfaces. Strips of zigzag tape are applied on the suction side at 5% of the local chord over the entire span and on the pressure side at 10% of the local chord over the entire span.

The low-speed experimental tests are conducted in the Open Jet Facility of Delft University of Technology. The facility is a closed-circuit, atmospheric wind tunnel capable of producing a maximum speed of 30 m/s. A side view of the wind tunnel setup is presented in Fig. 3. As a peniche is found to add flow complexity and measurements uncertainties [11, 12], it is not used between the model and the reflection plane. A 15 mm clearance gap is present between the model and the reflection plane to allow for rotation of the model without touching the reflection plane. The interaction effects between the boundary layer of the wind-tunnel walls and the model are mitigated by offsetting the reflection plane and the bottom wall of the wind tunnel outlet. A 400 mm offset is present between the reflection plane and the splitting plane. The splitting plane also acts as a shielding component to minimize the aerodynamic interaction between the airflow and the 6-axis balance, which is used to collect measurements. The balance is installed on a turning table to numerically control the angle of attack. Elliptical leading edges are mounted on the front side of the reflection plane to avoid vortex shedding from the sharp corner of the reflection plane itself, which may influence the aerodynamics of the wing, and to allow the development of a fresh boundary layer over the reflection plane. The model support beam is shielded below the reflection plane to minimize the effect of the airflow on the balance measurements. A picture of the experimental setup is presented in Fig. 4.

Aerodynamic forces and moments are recorded by means of a 6-axis balance at a sampling rate of 2 kHz. The measurement time is set to 15 seconds. Measurements are collected in the angle of attack range from -10 to 35 degrees at an airspeed of 20 m/s. The aerodynamic effects of the deflections of the three control surfaces are measured both by deflecting each surface individually as well as by deflecting multiple control surfaces at the same time. The most inboard control surface, referred to as CS1, is deflected from -10.5 to 12.2 degrees. The central control surface and the third control surface, referred to as CS2 and CS3, respectively, can be deflected between -15.2 and 17.8 degrees.

The measured forces and moments are unbiased using the biases collected at the beginning and at the end of each run assuming the bias increases linearly over time. Aerodynamic coefficients are generated from the balance measurements. The resulting data points are subsequently curve-fitted using a *smoothingspline* approach. A default smoothing parameter equal to 0.99 is used. For the flight mechanics analysis, the data is interpolated on 95 points which results in a resolution slightly lower than 0.5 degrees on the angle of attack. The derivatives of the aerodynamic coefficients are calculated using a first-order central-differencing scheme on the fitted data for the prediction of the aerodynamic center location in longitudinal and spanwise directions.

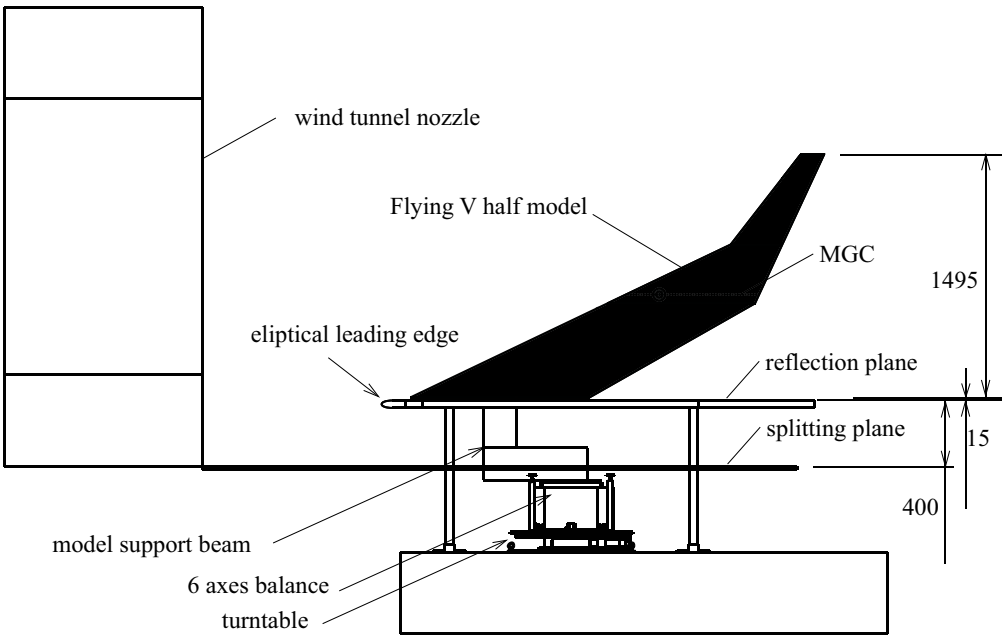

Fig. 3 Side view of experimental setup. Dimensions in millimeters

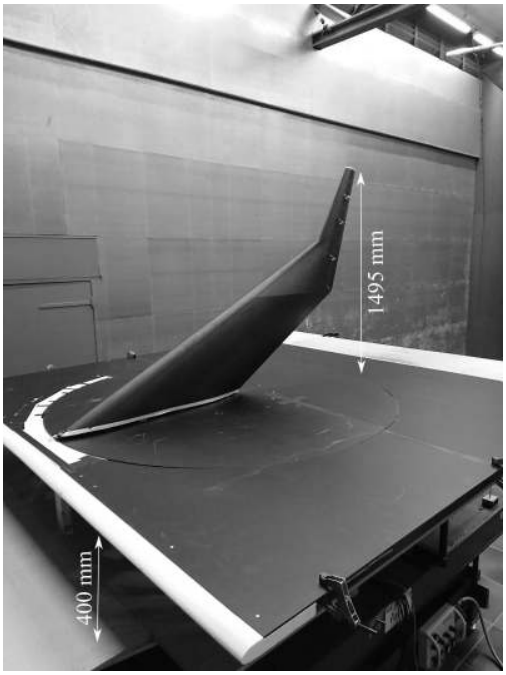

Fig. 4 Side view of the experimental setup.

C. Trim Analysis

As the scaled model will feature three independent elevons, the vehicle can be considered as a *multi-redundant control-surfaces* vehicle [13]. Trimming can therefore be performed in various ways. For example, one could trim by using just one control surface with a high deflection angle, or by using all control surfaces combined with a low deflection angle. In this paper, it is assumed that the most outboard control surface (CS3) is used primarily for roll control and its therefore excluded in the trim analysis. The trim problem is formulated in the body frame of reference (BFR) under the assumption of symmetric flight in order to identify the maximum achievable angle of attack with the available control authority while taking into account static stability requirements.

The equations of motion for symmetric flight are related the linear and rational accelerations to the aerodynamic forces and moments as follows:

$$\begin{cases} \dot{u} = \dfrac{q_\infty S}{m}\left[C_{X_\mathrm{A}} + C_{X_\mathrm{T}}\right] - g\sin\theta = 0 \\ \dot{w} = \dfrac{q_\infty S}{m}\left[C_{Z_\mathrm{A}} + C_{Z_\mathrm{T}}\right] + g\cos\theta = 0 \\ \dot{q} = \dfrac{q_\infty S\bar{c}}{I_{yy}}\left[C_{M_\mathrm{A}} + C_{M_\mathrm{T}}\right] = 0 \end{cases} \tag{1}$$

Here, subscripts "A" and "T" represent "aerodynamic" and "thrust", respectively. The mass of the aircraft is denoted with m, while θ is the pitch attitude angle. The aerodynamic forces and moments are a function of the angle of attack, α as well as the control surface deflection angles, i.e. δ_{CS1}, δ_{CS2}. The thrust-related coefficients are related to the throttle setting, (δ_{eng}), the location of the engine with respect to the center-of-gravity (CoG), and the incidence of the engine with respect to the X-axis of the aircraft (μ_{eng}):

$$\begin{cases} C_{X_\mathrm{T}} = \dfrac{T\left(\hat{\delta}_{\mathrm{eng}}\right)\cos\mu_{\mathrm{eng}}}{q_\infty S} \\ C_{Z_\mathrm{T}} = \dfrac{T\left(\hat{\delta}_{\mathrm{eng}}\right)\sin\mu_{\mathrm{eng}}}{q_\infty S} \\ C_{M_\mathrm{T}} = C_{X_\mathrm{T}}\dfrac{z_{\mathrm{CoG}} - z_{\mathrm{eng}}}{\bar{c}} + C_{Z_\mathrm{T}}\dfrac{x_{\mathrm{CoG}} - x_{\mathrm{eng}}}{\bar{c}} \end{cases} \tag{2}$$

The thrust force, T, represents the installed thrust force produced by the engine, i.e. it is the resultant of the thrust produced by the engine minus the drag produced by the cowling. The aerodynamic interaction between the engines and the aerodynamics of the configuration is not modeled.

The system of equations presented in Eqs. (1) is numerically solved in MATLAB for a given location of the center-of-gravity, flight speed, and flight path angle. The angle of attack, α, the deflections of the inboard and central control surfaces, $\hat{\delta}_{\mathrm{CS1}}$ and $\hat{\delta}_{\mathrm{CS2}}$, and the power setting of the engines, $\hat{\delta}_{\mathrm{eng}}$ are used as control variables. The control parameters of the control surfaces are used in a dimensionless form as CS1 and CS2 present different gear ratios and different maximum and minimum deflection angles. The deflection angles in degrees are then calculated based on the control parameter $\hat{\delta}_{CS_i}$ and a function f_{CS_i} as presented in Eq.(3).

$$\delta_{CS_i} = f_{CS_i}\left(\hat{\delta}_{CS_i}\right) \tag{3}$$

As the number of equations is less than the number of variables, an additional equation is defined to the control surface deflection of the center control surface (CS2) to the inboard control surface (CS1) according to:

$$\mathrm{CSDR} = \frac{\hat{\delta}_{CS2}}{\hat{\delta}_{CS1}} \tag{4}$$

where CSDR is the control surface deflection ratio, which is an input for this method. If CSDR = 1, it implies that the control parameters $\hat{\delta}_{\mathrm{CS1}}$ and $\hat{\delta}_{\mathrm{CS2}}$ will be equal but the actual deflection angles of the control surfaces will be different due to the different gear ratios. The use of an unitary value of CSDR results in the use of the full control authority.

The bounds on the control variables, make sure that the aircraft cannot be trimmed in all conditions. Particularly at low-speed conditions and/or more forward CoG positions balance is not possible. Additionally, when solving Eq. (1)

results in a trimmed aircraft, it does not necessarily ensure a stable aircraft. An inequality constraint is implemented to ensure that the static stability margin does not exceed a selected minimum static stability margin, i.e.:

$$C_{M_\alpha} \leq C_{M_\alpha}|_{\text{ref}} \tag{5}$$

where C_M is measured with respect to the CoG location.

III. Verification of Results

As noted in the introduction of this paper, the goal of this wind tunnel test is to assess the longitudinal stability and control parameters of the subscale Flying V. However, as a half-model is tested in open-jet wind tunnel, the question arises how representative the wind tunnel results are for the full-span flight test article. This question is addressed in this section.

A. Wind Tunnel Corrections

The first step to relate wind tunnel results to free-flight conditions is to apply wind tunnel corrections to the collected measurements. However, in this case no wind tunnel corrections are applied to the collected data as no correction method has been identified in the open literature for wind tunnel tests similar to the one at hand. The streamline curvature corrections identified in literature [14] are developed under the assumption of two dimensional flow and a non-cranked aerodynamic surfaces, which is not the case for the tested model. By considering the overall dimensions of the model, i.e. 2.5 m long and 1.5 m high, the application of a single constant global correction factor, either for streamline curvature or for dynamic pressure, is not justified. Based on these considerations, the airspeed is assumed to be constant over the entire wing and the flow of the open-jet wind tunnel fully developed over the entire setup. Qualitatively, the major effect due to wind tunnel testing in an open jet wind tunnel is reported as a mismatch between the geometric and the aerodynamic angle of attack as reported by Barlow et al. [14]. The effect on the outcome of the presented investigation would result in an underestimation of derivatives of forces and moments coefficients with respect to the angle of attack, therefore leading to conservative estimations.

B. Wind Tunnel Data Repeatability Analysis

To test the repeatability of the the wind-tunnel measurements, two data sets related to the deflection of the outboard control surface (CS3) have been repeated. The first repeated data set (Data set 1), is representative of a model polar between -10 and 35 degrees. At each angle of attack a complete sweep of control-surface deflections is performed on CS3, with the second control surface fixed at -6.5 degrees. The first data set consists of 220 measurements, i.e. 110 per repetition. The second, data set (Data set 2) is representative of a model polar between -10 and 20 degrees. At each angle-of-attack, a complete sweep of deflections is performed on the third control surface, with the second control surface fixed at -9.2 degrees. The second data set consists of 140 measurements, i.e. 70 per repetition.

The deviations of the measurements with respect to the mean value are computed per data set. These deviations are used to evaluate the confidence intervals [15] using a Student's t-distribution under the assumption that neither the angle of attack nor the control surface deflection influences the quality of the measurements. The deviations and the confidence intervals are presented in Fig. 5 and 6. Four horizontal lines are presented in the deviation plots, indicative of the 95% (dashed lines) and 99% (dot-dashed lines) confidence intervals. Based on these results, it is concluded that the 99% confidence intervals for C_M, C_L, and C_D are 30, 78, and 16 counts*, respectively. Even though a wider spread of deviation can be observed at some angles of attack, the experiment is deemed to be repeatable.

C. Comparison to CFD Results

To provide some form of validation, the wind tunnel results are compared to CFD simulations of the model in free-flight conditions to compare the forces and moments. The geometry of the wing is discretized using ANSYS® meshing. The wing is split in 700 divisions in spanwise-direction and 260 in chordwise-direction both on the suction and pressure side of the wing. An inflation layer is built around the wing using 39 layers, a first height equal to $3{\cdot}10^{-6}$, to simulate y^+ smaller than 1, and a geometric growth rate equal to 1.2. The dimensions of the computational domain are 50x25x50 meters to minimize the influence of the velocity boundary condition on the solution. The volume of the domain is meshed with an unstructured grid. Grid density is controlled in proximity of the aerodynamic surface to increase the

*1 count represents 1×10^{-4}

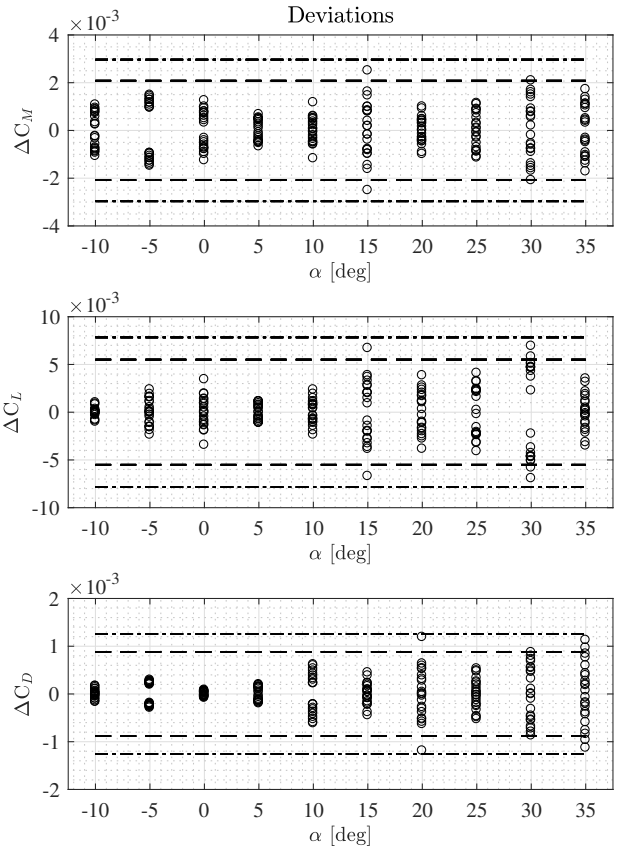

Fig. 5 Data repeatability. Data-set 1.

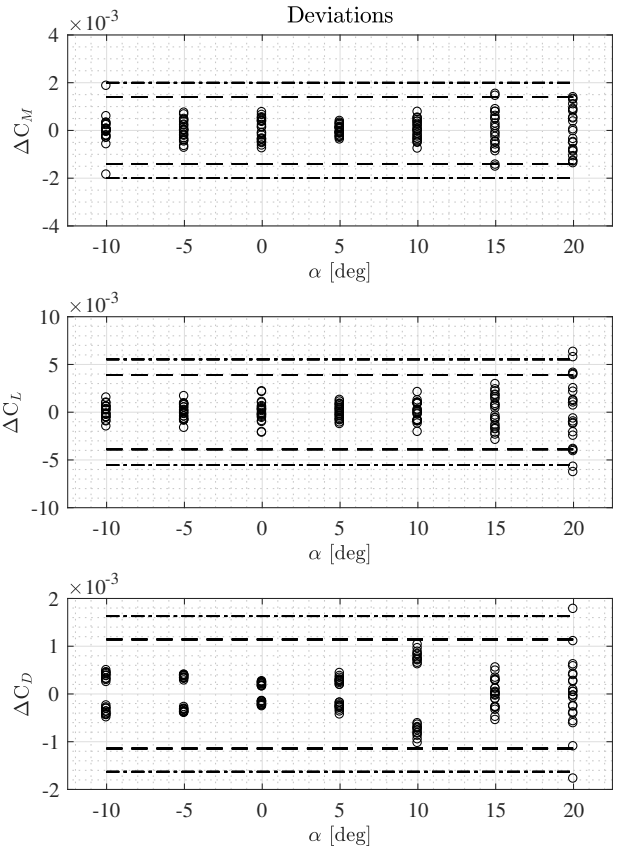

Fig. 6 Data repeatability. Data-set 2.

resolution of the grid in that region. The dimensions of the refinement zone are 6x2x3.5 meters (i.e. 7.3x2.4x4.2 $\bar{c}$). The dimension of the cells in the refinement region of the mesh is limited to $2.5{\cdot}10^{-2}$ m. The generated mesh features a total of 72.1 million cells. An isometric view of the computational domain is presented in Fig. 7. The wing surface is modeled as a no-slip wall, while on the symmetry plane of the domain symmetric boundary conditions are applied. The outlet surface of the domain is modeled as a pressure outlet, while on the inlet surfaces the velocity vector is specified both in magnitude and direction.

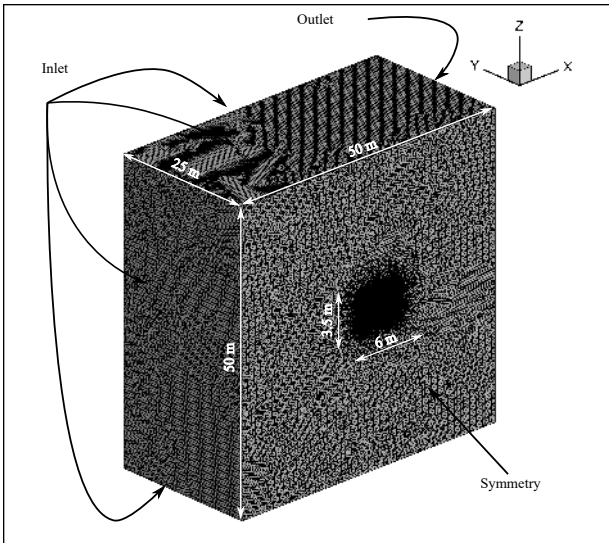

Fig. 7 Computational domain, dimensions, and boundary conditions.

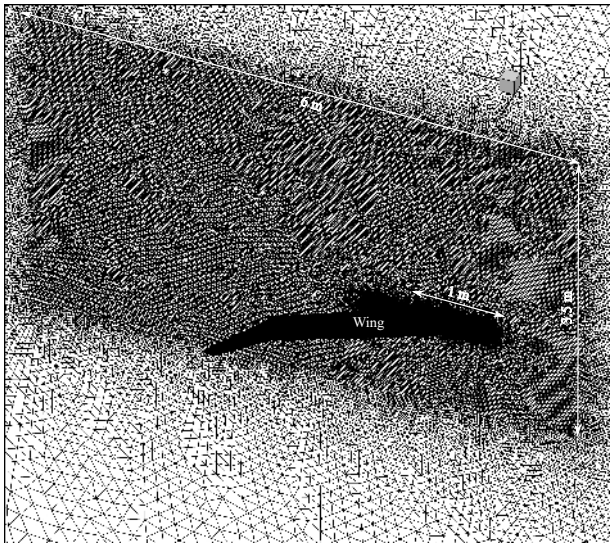

Fig. 8 Enlargement of the computational domain on the refinement zone.

The free-stream velocity is set to 20 m/s at standard ISA conditions. Turbulent intensity is set to 0.5% according to previous measurements [16]. The turbulent length scale is set to 0.02 m. A pressure-coupled scheme is used to solve the pressure field using the pseudo-transient formulation. Second-order schemes are used for all the flow variables. Gradients are calculated using the Green-Gauss node-based option to ensure a second-order interpolation on the non-orthogonal grid. Finally, the simulations are performed using the Spalart-Almaras one-equation eddy viscosity model [17]. The *curvature correction* option is incorporated as well as the *strain/vorticity-based* production term, proposed by Dacles-Mariani et al. [18], to prevent build-up of turbulence viscosity in vortex cores [19].

The comparison of lift, drag, and pitching moment coefficients between the wind tunnel and the CFD analyses are presented in Fig. 9 up to an angle-of-attack of 20 degrees. The lift curve shows excellent correlation between the two methods, with a slight over-predictions in terms of lift coefficient of about 12%. This could be attributed to the fact the wind tunnel model was equipped with zigzag strips on either side, artificially increasing the boundary-layer thickness and reducing the effective curvature of the model. The presence of the gap between the root section of the wing and the symmetry plane can also reduce the lift on the inboard side of the wing. Finally, the effective angle-of-attack of the wind-tunnel model might have been lower than the geometric angle-of-attack due the interference between the model and the wind tunnel walls.

The drag coefficient estimations are lower for the CFD analysis between 0 and 15 degrees but shows relatively good agreement with the measurements at higher angles of attack. The higher (friction) drag coefficient of the wind tunnel model is attributed to the momentum-loss induced by the zig-zag strips on either side of the wing. The steep drag rise with angle of attack occurs for both the wind tunnel model and the CFD analysis, increasing the confidence in these results.

The largest discrepancies between the wind-tunnel measurements and the CFD results are found in the pitching moment coefficients. While the pitching moment coefficient at zero angle of attack is estimated within 7% of the measured value, the slope of the pitching moment coefficient with angle-of-attack is much steeper in the CFD results than in the measurements. Furthermore, the CFD predictions also show an additional peak in the moment curve around 7.5 degrees angle-of-attack, which is absent in the measurements. Finally, a start of the pitch break is visible between 15 and 17.5 degrees for the CFD results, while this happens at 19 degrees for the wind-tunnel model. Obviously, the

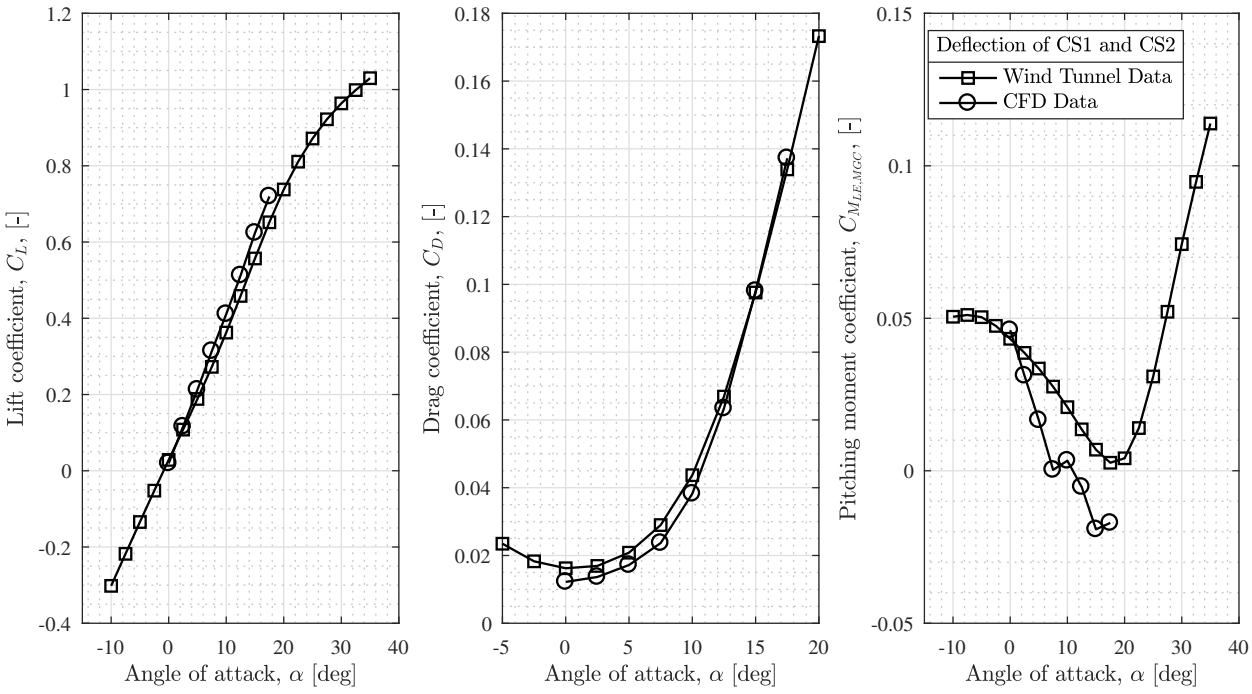

Fig. 9 Comparison of the CFD and wind tunnel data in terms of lift, drag, and pitching moment coefficient. $V_\infty \approx 20$ m/s. $Re_{\bar{c}} \approx 1 \cdot 10^6$. $\rho \approx 1.22$ kg/m^3.

aerodynamic center, as predicted by the CFD lies further rearwards compared to wind-tunnel model. This, combined with the somewhat higher lift coefficient predicted by CFD increases the absolute value of the pitching moment for a given angle of attack.

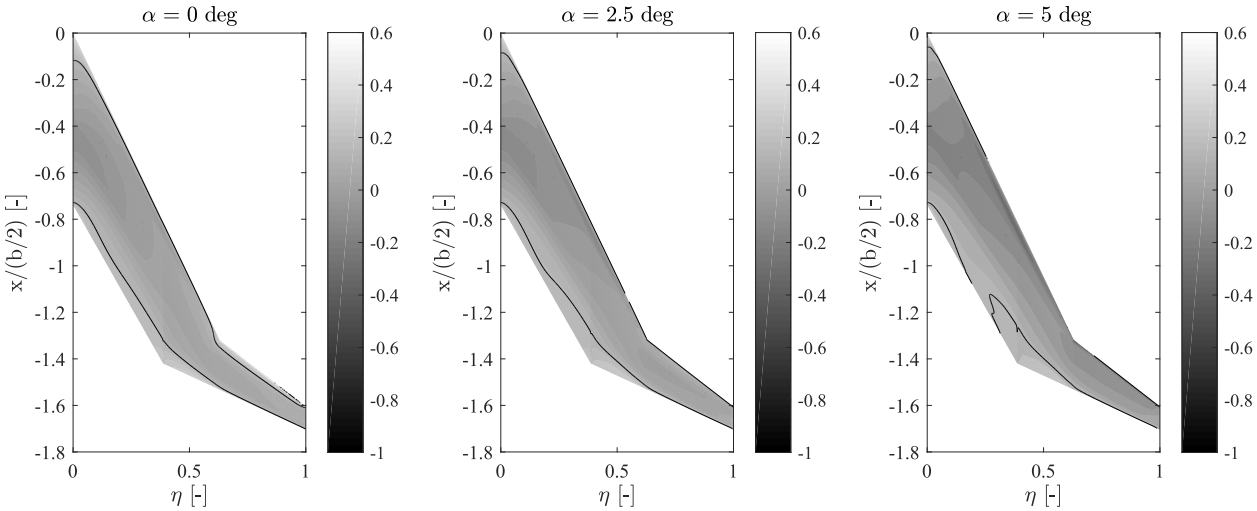

Fig. 10 Pressure coefficient contours on the suction side at 0, 2.5, and 5 degrees angle of attack. Solid black line: $C_P = 0$.

Despite the discrepancies between the presented aerodynamic coefficients predicted by CFD analyses and those extracted from the wind tunnel measurements, the aerodynamic coefficients are predicted in the same order of magnitude. The largest source of error is due to the influence of the gap between the root-section and the reflection plane. Its effect on the results should be further investigated. However, from a qualitatively point of view, the experiment is deemed to be a good representation of the free-flying model. It is therefore concluded, that the results from the aerodynamic

experiments can be used to make an assessment of the stability and trim properties of the aircraft.

IV. Results

A. Aerodynamic Coefficients

The half-model is exposed to an airflow of 20m/s over a range of angles-of-attack between -10° and +35°. Three conditions are considered: 1) full up deflection of CS1 and CS2, 2) all controls in neutral position (i.e. clean configuration), and 3) full down deflection of CS1 and CS2. The resulting lift, drag and pitching moment curves are presented in Fig. 11. The reference point for the estimation of the pitching moment coefficients is the projection of the leading edge point of the mean geometric chord onto the symmetry plane of the model (see also Table 1).

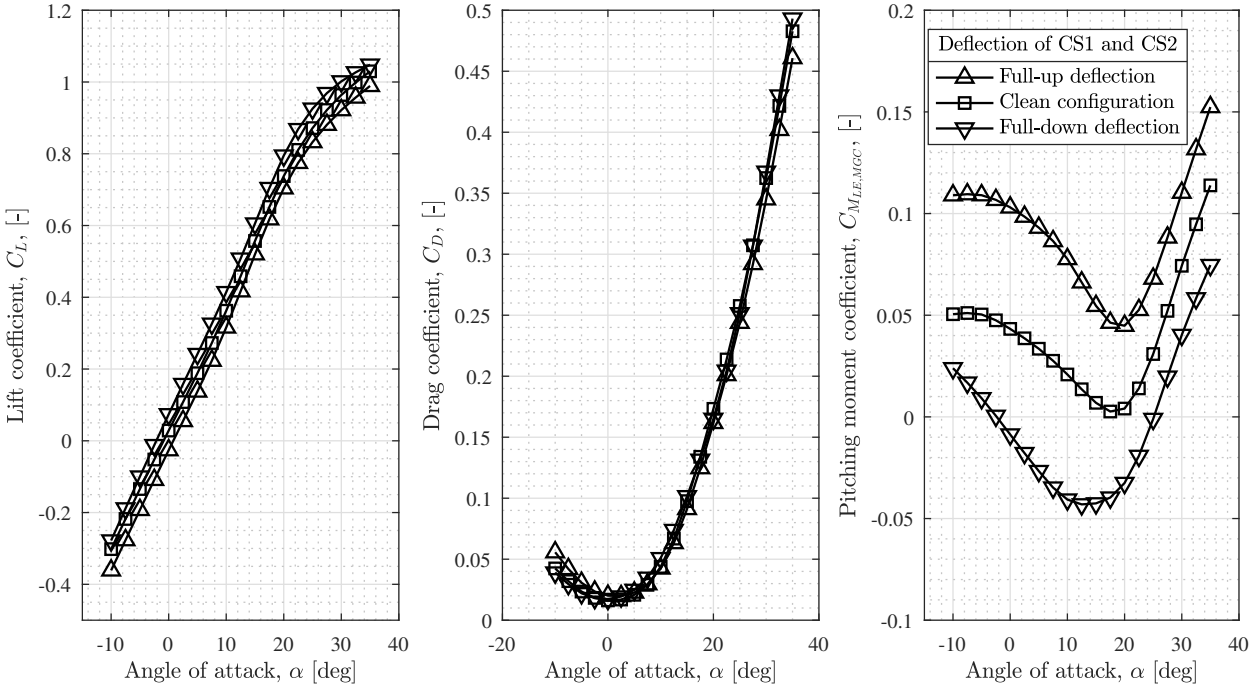

Fig. 11 Lift, drag, and pitching moment coefficient curves. Pitching moment reference point located at the leading edge point of the mean geometric chord of the tested model. Aerodynamic effects of the deflections of the inboard (CS1) and central (CS2) control surfaces displayed. Outboard control surface (CS3) non-deflected. $V_\infty \approx 20$ m/s. $Re_{\bar{c}} \approx 1 \cdot 10^6$. $\rho \approx 1.22$ kg/m^3.

Within the investigated range of angles of attack, the Flying V configuration present lift characteristics similar to those of low-aspect-ratio wings [20], with a $C_{L_\alpha} \approx 2.3$ per radian. A very gradual loss in lift gradient is shown starting around 20° and peaking around 35°. At high angles of attack, the tested model performs aerodynamically similarly to a delta wing by generating a set of vortices that contribute to the vortex lift. While the effect of the control surface deflection on the lift and drag curves is almost negligible, the control surfaces do have a strong impact on the pitching moment coefficient. An unstable pitch break is observed in the pitching moment curve due to a rapid forward displacement of the aerodynamic center with angle of attack. The pitch breaks takes place at about 15, 18, and 20 degrees angle of attack for full-down, neutral, and full-up deflections, respectively. The dependence of pitch-up break tendency on the deflection angle of the control surfaces highlights an influence of control surface deflection on the position of the aerodynamic center at large angles of attack.

B. Control Derivatives and Mutual Interaction Effects

To compute the stability and control derivatives, curves are fitted to the data points. The mean coefficient of determination of the 154 interpolations performed on the dataset to increase the resolution of the data from 5 to 2.5

degrees is equal to 0.9988. Contours of the pitching moment derivative with respect to control surface deflection of the inboard (CS1) and central (CS2) control surfaces, respectively, are presented in Fig. 12 and 13. The pitching-moment control power contours are presented in the investigated range of control surface deflection for full-up, neutral, and full-down deflection of the adjacent control surface.

The two inboard control surfaces appear to be always effective within the tested range of angles of attack and deflections. Although reductions in the pitch control power occur at larger deflections, greater control authority could still be achieved by increasing the maximum deflections the control surfaces. In general, reductions in pitching moment control power of either of CS1 or CS2 are observed as the deflection of adjacent control surface increases. A positive control power region is estimated when CS1 is deflected full-down for angles of attack between -10 and -7.5 degrees. The maximum values of pitching moment control derivative of CS1 are estimated in the range of angles of attack between 10 and 20 degrees.

To highlight the interaction effects between the control surfaces, a dimensionless metric, referred to as the mutual interaction factor, ξ_{ij}, is defined as follows:

$$\xi_{ij} = \frac{C_{M_{\delta_{CS_i}}}|_{\delta_{CS_j}=\delta^*}}{C_{M_{\delta_{CS_i}}}|_{\delta_{CS_j}=0}} \tag{6}$$

The mutual interaction factor metric ξ_{ij} represents the ratio between the pitching moment control derivative of the surface i-th for a non null-deflection of the surface j-th and the pitching moment control derivative of the surface i-th for zero-deflection of the surface j-th.

The mutual interaction factor metrics ξ_{ij} are presented in Fig. 14 for the two inboard control surfaces for full-up and full-down deflections of the j-th surface. Based on the data presented in Fig. 14, the mutual interaction factor ranges between 0.8 and 1.2 in the angle of attack range between 0 and 10 degrees, both for negative and positive deflection angles of the j-th control surface, thus highlighting that within this range of angles of attack the deflection of the control surfaces do not severely influence the flow structure over the aerodynamic shape. For angles of attack larger than 10 degrees, the mutual interaction factor assumes more significant values. While negative deflections of the j-th control surfaces, induce the pitching moment control derivative of the i-th control surface to increase, $\xi_{ij} > 1$, for positive deflections of the j-th control surfaces produce the opposite effect, leading to a reduction in pitching moment control derivative of the i-th control surface, $\xi_{ij} < 1$.

Considering the negative deflections of the j-th surfaces (left column in Fig. 14) the mutual interaction factor achieves values between 1.2 and 2, which indicates the pitching moment control derivative increase between 20% and 100% with respect to the values computed with a zero deflection of the j-th control surface. On the other hand, when positive deflections of the j-th surface are considered (right column in Fig. 14) losses up to 80% in pitching moment control derivative are estimated.

The presented data suggest that the deflections of the control surfaces severely affect the direction and, possibly the breakdown of the vortical structures predicted by CFD analyses and observed during the wind tunnel campaign by means of oil-flow and smoke visualization technique.

1. Dependence of the Aerodynamic Center on Angle of Attack and Mixed Deflections of the Control Surfaces

The positions of the aerodynamic center are calculated within the tested ranges of angles of attack and deflections of the two inboard control surfaces. In Fig. 15, the identified locations of the aerodynamic center are plotted onto the planform view of the model for all the tested angles of attack relative to the cases of full-up, neutral, and full-down deflections of the inboard and central control surfaces.

In clean configuration, at zero angle of attack, and zero deflection of the control surfaces, the aerodynamic center of the tested model is located at 1.37 meters from the aircraft's nose. For angles of attack between -10 and 0 degrees, the longitudinal position of the aerodynamic center travels between 1.32 and 1.37 meters, an excursion of about 6% $\bar{c}$. Between 0 and 10 degrees angle-of-attack, the aerodynamic center travels from 1.37 to 1.39 meters, about 2% $\bar{c}$. Between 0 and 20 degrees, the combined deflection of the CS1 and CS2 can induce a maximum shift in the aerodynamic center of about 5 centimeters, about 6% $\bar{c}$, thereby producing non-negligible effects on the longitudinal static stability characteristics of the tested model.

In addition to Fig. 15, the longitudinal and spanwise locations of the aerodynamic center are presented as functions of the angle of attack in Fig. 16. These graphs highlight the effects of angle-of-attack and control-surfaces deflection on the aerodynamic coefficients of the tested model. Three intervals of angles of attack are found for which trends can be

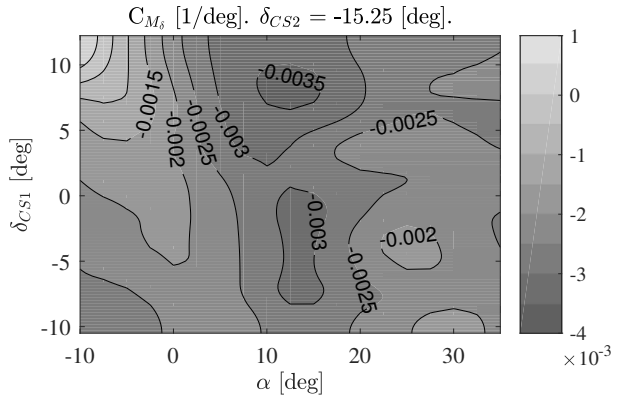

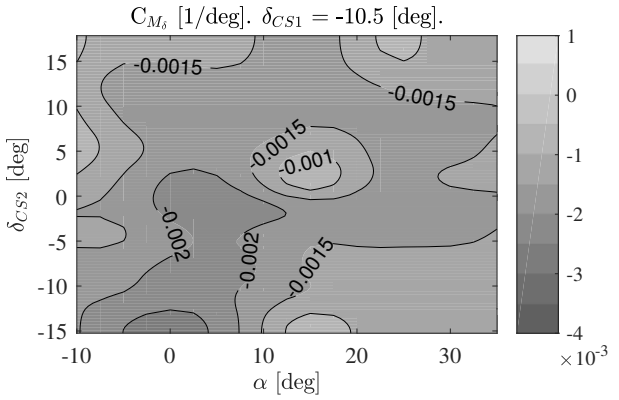

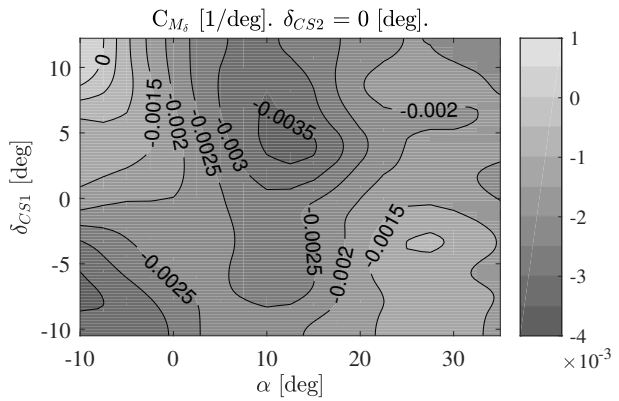

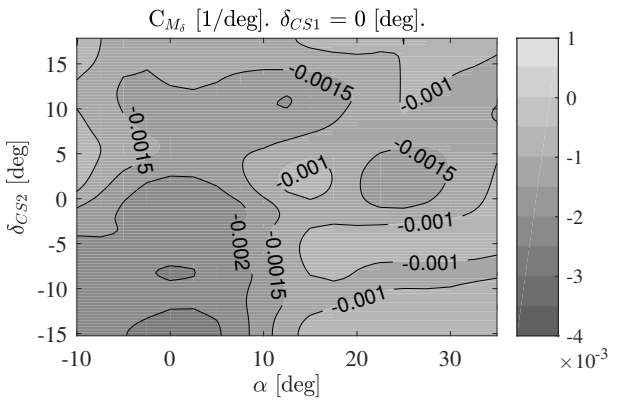

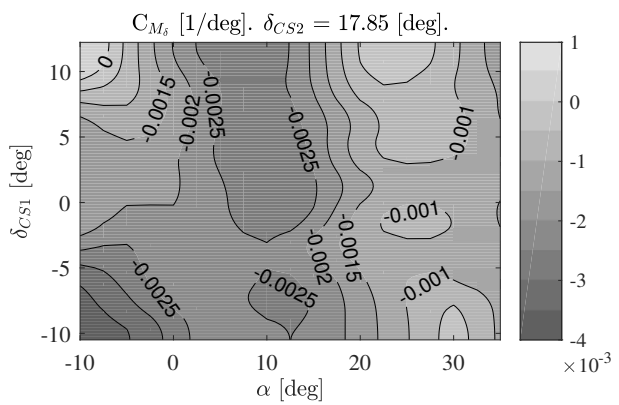

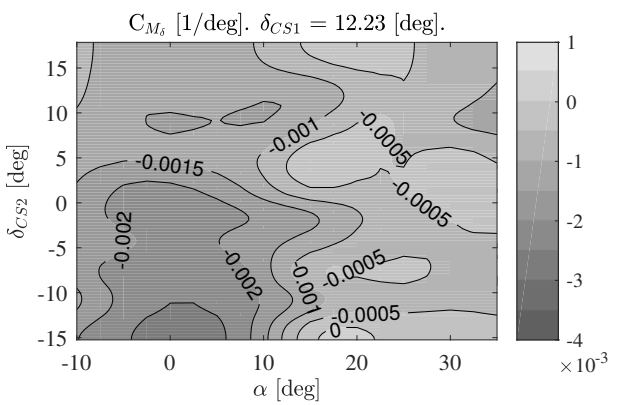

Fig. 12 Pitching moment control power contours of the inboard control surface (CS1) at full-up, null, and full-down deflections of the central control surface (CS2). $V_\infty \approx 20$ m/s. $Re_{\bar{c}} \approx 1 \cdot 10^6$. $\rho \approx 1.22$ kg/m^3.

Fig. 13 Pitching moment control power contours of the central control surface (CS2) at full-up, null, and full-down deflections of the inboard control surface (CS1). $V_\infty \approx 20$ m/s. $Re_{\bar{c}} \approx 1 \cdot 10^6$. $\rho \approx 1.22$ kg/m^3.

identified in relationship to fixed deflections of the control surfaces. The bounds of the three intervals (I) are presented as mean of vertical dashed gray lines in Fig. 16:

$$\begin{aligned} I_1: \quad & \alpha \in [-10, 12] \quad \text{deg} \\ I_2: \quad & \alpha \in \langle 12, 27] \quad \text{deg} \\ I_3: \quad & \alpha \in \langle 27, 35] \quad \text{deg} \end{aligned} \tag{7}$$

The effect of angle of attack and control-surface deflection on the longitudinal and lateral location of the aerodynamic center is described for the three identified angle-of-attack intervals:

- $\alpha \in I_1$: the aerodynamic center shifts aft and inboard when the angle of attack increases. Negative deflections of

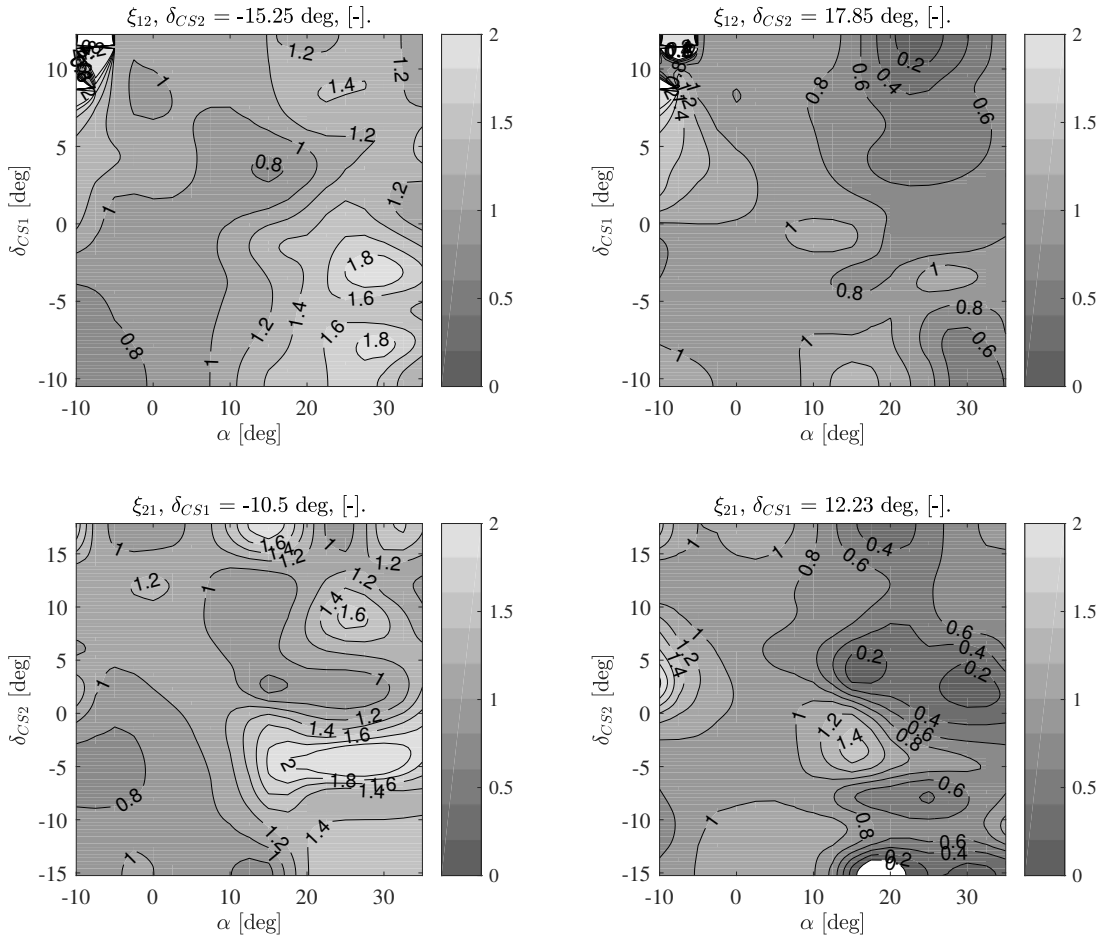

Fig. 14 Contours of the mutual interaction factor metrics ξ_{ij} of the two inboard control surfaces CS1 and CS2. As defined in Eq. (6), the metric is representative of the ratio between the pitching moment control derivative of the control surface i-th for a non-null deflection angle of the j-th control surface with respect to the same quantity estimated for a null deflection of the j-th surface. $V_\infty \approx 20$ m/s. $Re_{\bar{c}} \approx 1 \cdot 10^6$. $\rho \approx 1.22$ kg/m^3.

the first control surface induce an aft and outboard shift. Positive deflections of the first control surface induce a forward shift and inboard. When the first control surface is deflected upwards and the angle of attack approaches 12 degrees, the aerodynamic center starts shifting forward.

- $\alpha \in I_2$: the aerodynamic center shifts inboard and forward when the angle of attack increases. Negative deflections of the first control surface cause the aerodynamic center to shift inboard and forward. Positive deflections of the first control surface cause the aerodynamic center to shift outboard and rearward.
- $\alpha \in I_3$: the aerodynamic center tends to stay in the same location for zero and negative deflections of the first control surface. Positive deflections of the first control surface cause the aerodynamic center to shift forward and inboard. This inboard shift is amplified when the second control surface is positively deflected as well. At 35 degree angle of attack and $\delta_{CS1} = 17.8°$, the aerodynamic center travels forward over 0.07 m, i.e. 8.5% $\bar{c}$ between the minimum and maximum deflection of the inboard control surface. The spanwise travel is even larger, i.e. 0.17 m, or 11% of the wing's semi-span.

Although no flow visualization has been collected, a physical explanation for the forward shifting of the aerodynamic center at 35 degrees with both CS1 and CS2 fully positively deflected has been hypothesized. The positive deflections both of CS1 and CS2 might may cause the vortex released at the kink to flow in a more streamwise direction, thus causing a loss of effectiveness on the most outboard sections of the wing, which might suffer with leading edge stall. The presented hypothesis is supported by the fact that the aerodynamic center longitudinal location shifts forward as the second control surface passes from negative to positive deflections. The presented hypothesis is also in agreement with

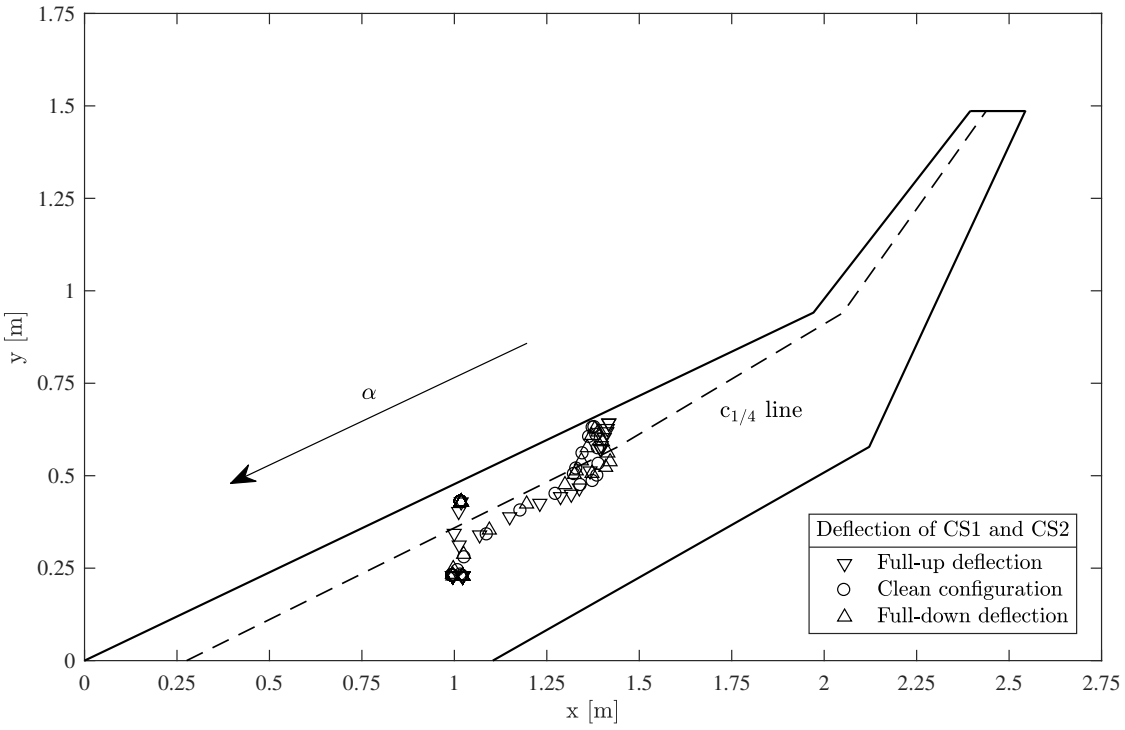

Fig. 15 Travelling of the aerodynamic center position on the half-wing planform top view within the investigated range of angles of attack at different deflections. Dashed line: quarter chord line.

the spanwise shifting tendency of the aerodynamic center at 35 degrees. A possible verification, beside the use of flow visualization techniques, may be the collection of balance data of CS3 data at 35 degrees for full positive deflections of CS1 and CS2 to check whether the most outboard control surface is still effective or not when deflected negatively.

C. Influence of the Longitudinal Location of the center-of-gravity on Max Lift Coefficient in Trimmed Conditions

Based on the collected aerodynamic data and on the simplified engine model, the influence of the longitudinal location of the center-of-gravity on the maximum lift coefficient achievable in steady-state flight in trimmed condition is estimated both in power-off and power-on conditions to identify the minimum speed. The entire control power is used to estimate the landing speed for future SFT activities, assuming a unitary CSDR value.

The results are obtained by constraining the arbitrary value of C_{M_α} equal to -1.5 $\cdot 10^{-3}$ 1/deg, which results in a static stability margin equal to $x_{\text{ac}} - x_{\text{CoG}} = 0.044\bar{c}$. The pitching-moment derivative is calculated from the wind tunnel pitching moment curves to account for the effects of the deflections on the location of the aerodynamic center during the trim analyses. The analysis is performed assuming a mass of the model equal to 25 kg. To identify the most forward and rearward location of the center-of-gravity, a maximum landing airspeed equal to 20 m/s is selected, which results in a required lift coefficient of about 0.54. The results of the analyses are presented in Fig. 17.

It can be seen that the trimmed maximum lift coefficient (top graph in Fig. 17) is 0.68, giving rise to a 12% margin in the stall speed of the aircraft. Note that the pitching-moment derivative remains negative, meaning the aircraft is statically stable. The maximum trimmed lift coefficient decreases from 0.68 to 0.66 when power-on condition is considered. This is a 3% reduction, still the minimum speed of the configuration in power-on configuration would be equal to 18 m/s, only 1,4% larger than the one estimated in power-off conditions. The center-of-gravity location for the power-off and power-on configuration can be located in the interval of [-7.5%; 0.5%] $\bar{c}$ and [-6%; 1%] $\bar{c}$, respectively, measured from the longitudinal location of the leading edge of the mean geometric chord of the configuration. The center-of-gravity excursion that allows a maximum landing speed of 20 m/s is reduced by 14% from power-off to power-on conditions, from 0.065 to 0.057 m. The best locations in terms of trimmed maximum lift coefficient for power-off and power-on conditions are located respectively at -4% $\bar{c}$ and at -2.7% $\bar{c}$ with respect to the leading edge of the mean geometric chord.

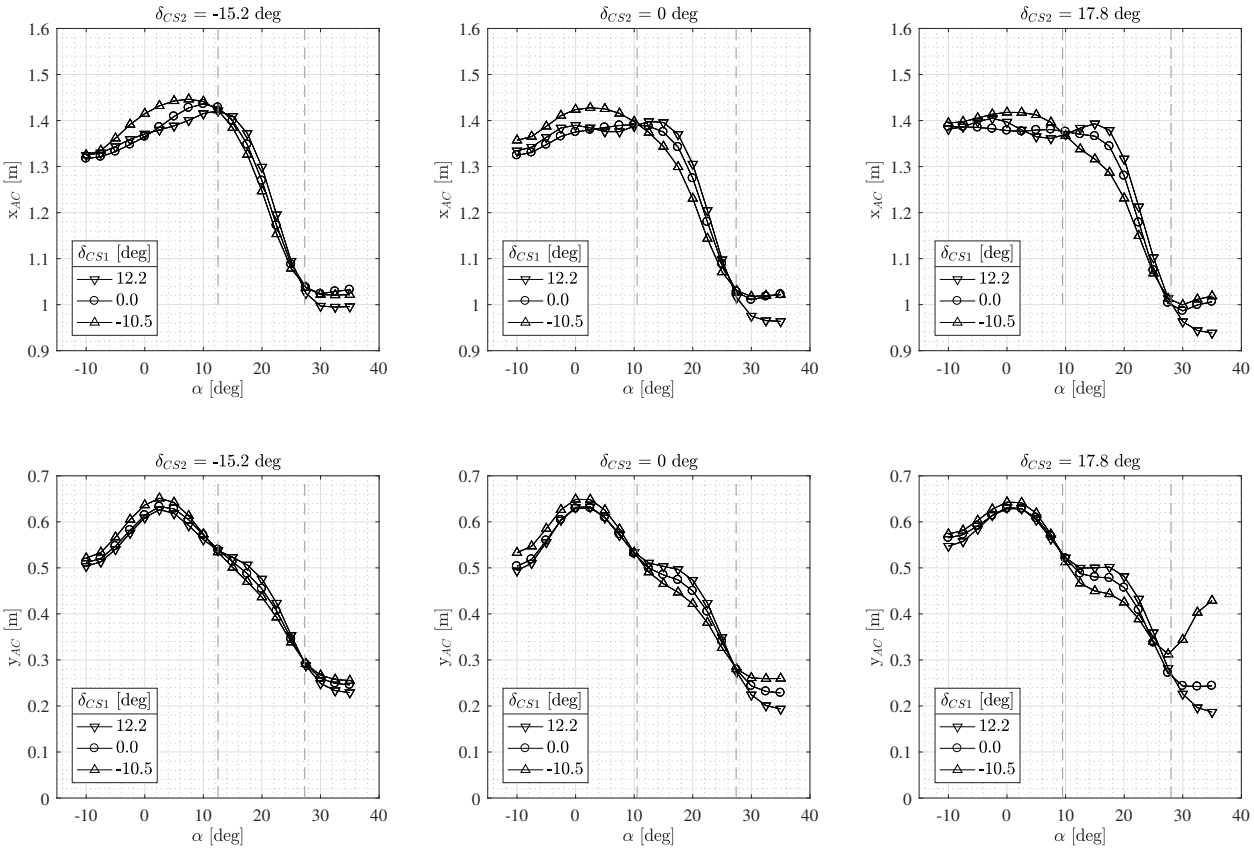

Fig. 16 Longitudinal and spanwise locations of the aerodynamic center over the tested half-wing as functions of the angle of attack for different control surface deflections.

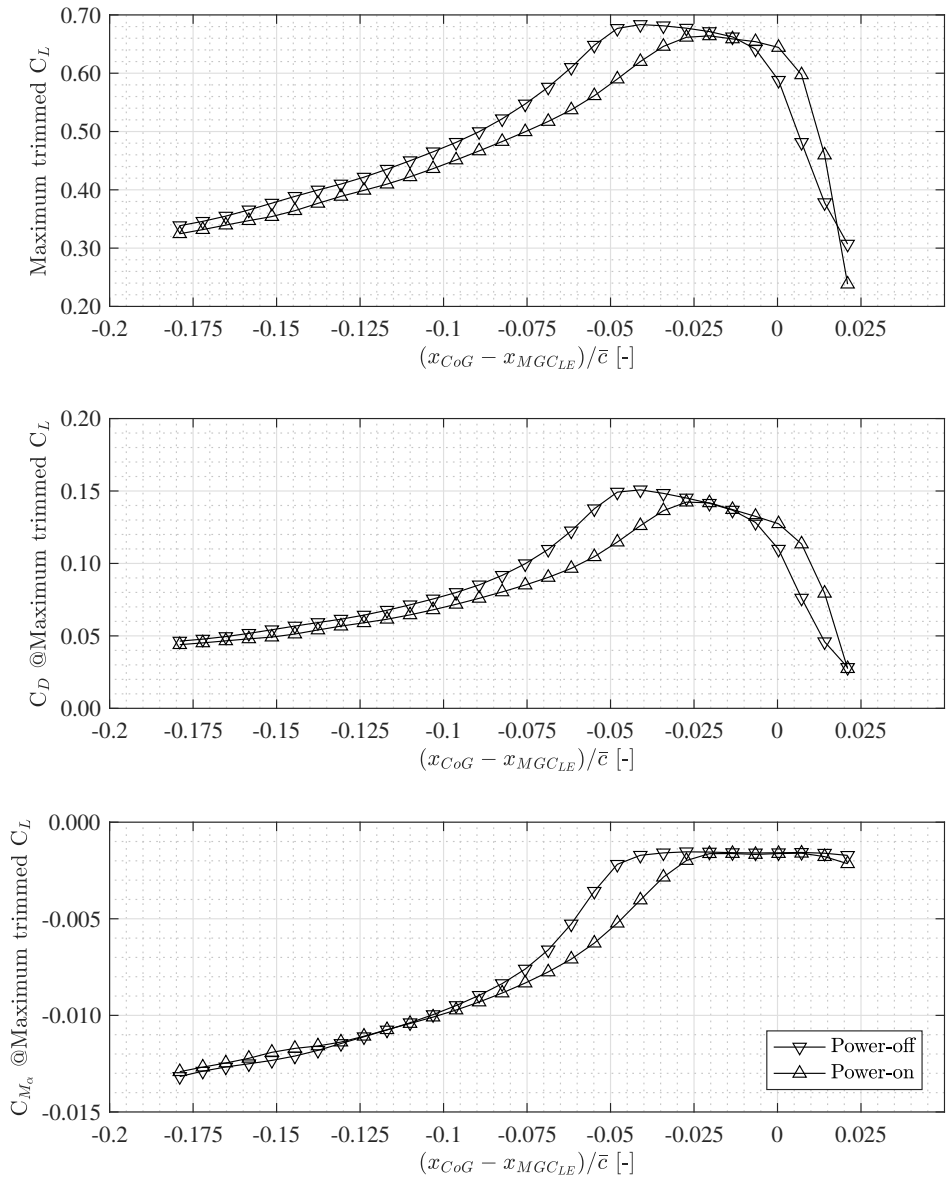

Fig. 17 Influence of the longitudinal location of the center-of-gravity on the maximum lift coefficient achievable in trimmed lift coefficient (top graph), drag coefficient in max lift (central graph), and angle of attack pitching moment derivative (bottom graph). The legend is shared among all the plots.

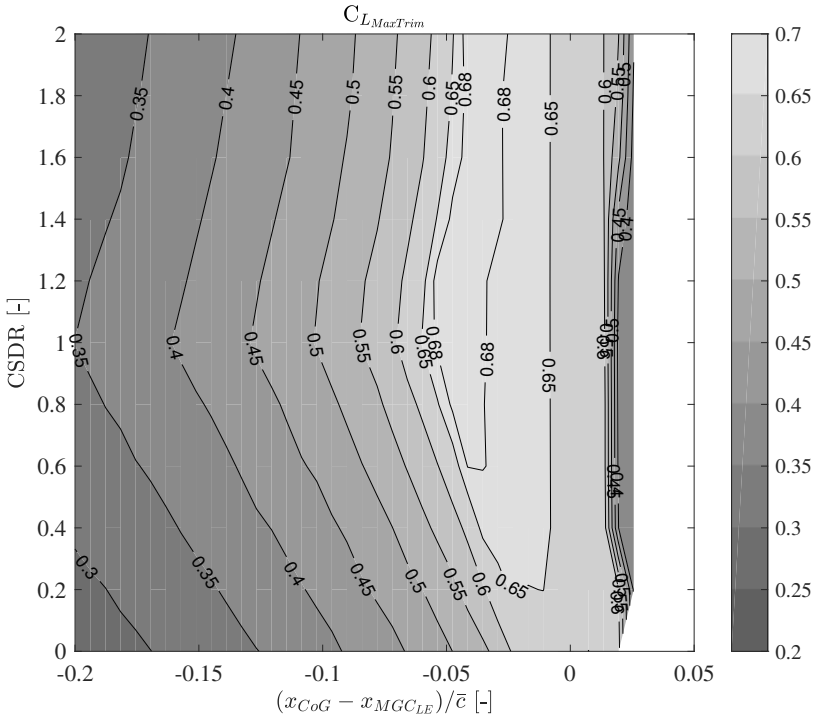

Fig. 18 Search to identify the combined effects of longitudinal center-of-gravity locations and CSDR values on the maximum lift coefficient in trimmed condition in power-off conditions.

A search in power-off conditions is performed to exclude the possibility that the trimmed maximum lift coefficient of the aft-locations of the center-of-gravity range is affected by the shift of aerodynamic center induced by the control surfaces. During the search both the CSDR value as well as the longitudinal location of the center-of-gravity assume different values. For this assessment, the CSDR values range between 0 and 2. The results of the search are presented in Fig. 18. It can be observed that the iso-$C_{L_{MaxTrim}}$ curves in Fig. 18 are almost vertical for the aft location of the center-of-gravity range indicating that the deflections of the control surfaces do not affect the maximum lift condition. On the other hand, for any forward-locations of the center-of-gravity, the trimmed lift coefficient is always maximized for unitary values of CSDR, then when the full control authority is used. Based on the results in Fig. 18 and the control power plots in Fig. 12 and 13, larger $C_{L_{MaxTrim}}$ values could be achieved for the forward location of the center-of-gravity range by decreasing the minimum deflection angles of CS1, thus the pitching moment control authority of CS1.

V. Conclusions and Recommendations

Wind-tunnel testing of a 4.6%-scale half-model of a Flying-V transport aircraft has been performed in the open-jet wind tunnel at Delft University of Technology. The experiments are found to be repeatable. The uncorrected wind tunnel results also correlate well in terms of lift and drag coefficients with the results from CFD simulations in the same operating conditions. However, the pitching-moment comparison reveals CFD simulations predict the aerodynamic center to be located more aft of the locations identified using wind tunnel data and earlier pitch-up break tendency is observed in CFD results. With the controls in neutral position, the maximum lift coefficient of 1.02 occurs at the maximum tested angle of attack (35 degrees). The aerodynamic center is shown to shift strongly as a function of angle of attack and, to a lesser extent, with control-surface deflection. The full longitudinal excursion od the aerodynamic center is as much as 55%$\bar{c}$. For angles of attack lower than 10 degrees the mutual interference of adjacent control surfaces is within ±20%. At angles of attack larger than 10 degrees, interference between adjacent control surfaces increases, inducing variation in the pitching moment control power as large as ±80%. The effects of the center-of-gravity location on the trimmed maximum lift coefficient are estimated and the center-of-gravity range is estimated under the constraint of an ultimate static stability margin equal to 4.4% $\bar{c}$ and a maximum landing airspeed of 20 m/s. The center-of-gravity is to be located in the interval of [-7.5; 0.5] %$\bar{c}$ in power-off conditions and in the interval of [-6%; 1%]$\bar{c}$ in power-on

conditions. These ranges could be forwardly expanded by increasing the gear ratio of the inboard control surface of the vehicle. The trimmed maximum lift coefficients are 0.68 and 0.66 in power-off and power-on conditions, respectively.

References

[1] Benad, J., "Technical report: Design of a commercial aircraft for high-subsonic speed as a flying wing configuration," *Airbus*, 2015.

[2] Faggiano, F. et al., "Aerodynamic Design of a Flying V Aircraft," *17th AIAA Aviation Technology, Integration, and Operations Conference*, 2017, p. 3589.

[3] Bolsunovsky, A.L. et al., "Flying wing-problems and decisions," *Aircraft design*, Vol. 4, No. 4, 2001, pp. 193–219.

[4] Martinez-Val, R. et al., "Conceptual design of a medium size flying wing," *Proceedings of the Institution of Mechanical Engineers, Part G: Journal of Aerospace Engineering*, Vol. 221, No. 1, 2007, pp. 57–66.

[5] Torenbeek, E., "Blended-wing-body and all wing airliners," *8th European Workshop on Aircraft Design Education*, 2007.

[6] Liebeck, R. H., "Design of the blended wing body subsonic transport," *Journal of aircraft*, Vol. 41, No. 1, 2004, pp. 10–25.

[7] Brown, M., and Vos, R., "Conceptual Design and Evaluation of Blended-Wing Body Aircraft," *Proceedings of the 2018 AIAA Aerospace Sciences Meeting*, Kissimee, FL, 2018.

[8] Vicroy, D., "Blended-wing-body low-speed flight dynamics: summary of ground tests and sample results," 2009.

[9] Vicroy, D., "X-48b blended wing body ground to flight correlation update," 2011.

[10] Goldthorpe, S. H. et al., "X-48b blended wing body flight test performance of maximum sideslip and high to post stall angle-of-attack command tracking," *AIAA Guidance, Navigation, and Control Conference*, 2010, pp. 1–17.

[11] Eder, S. et al., "Semi-span testing in wind tunnels," *25th International Congress of the Aeronautical Sciences: ICAS*, 2006, pp. 1–9.

[12] Skinner, S.N. and Zare-Behtash, H., "Semi-span wind tunnel testing without conventional peniche," *Experiments in Fluids*, Vol. 58, No. 12, 2017, p. 163.

[13] Garmendia, D. C. and Mavris, D. N., "Alternative trim analysis formulations for vehicles with redundant multi-axis control surfaces," *Journal of Aircraft*, 2015.

[14] Barlow, J. B. and Rae, W. H. and Pope, A., "Low-speed wind tunnel testing," 1999.

[15] Neyman, Jerzy, "X-Outline of a Theory of Statistical Estimation Based on the Classical Theory of Probability," *Phil. Trans. R. Soc. Lond. A*, Vol. 236, No. 767, 1937, pp. 333–380.

[16] Lignarolo, L. and Ragni, D. and Simao Ferreira, C. and van Bussel, G., "Turbulent mixing in wind turbine and actuator disc wakes: Experiments and POD analysis," *33rd Wind Energy Symposium*, 2015, p. 223.

[17] Spalart, P.R. and Allmaras, S. R., "A one-equation turbulence model for aerodynamic flows," *30th aerospace sciences meeting and exhibit*, 1992, p. 439.

[18] Dacles-Mariani, J. and Zilliac, G. G. and Chow, J. S. and Bradshaw, P., "Numerical/experimental study of a wingtip vortex in the near field," *AIAA journal*, Vol. 33, No. 9, 1995, pp. 1561–1568.

[19] Stokkermans, T. C. and van Arnhem, N. and Sinnige, T. and Veldhuis, L. L., "Validation and Comparison of RANS Propeller Modeling Methods for Tip-Mounted Applications," *2018 AIAA Aerospace Sciences Meeting*, 2018, p. 0542.

[20] Houghton, E. L. and Carpenter, P. W., *Aerodynamics for engineering students*, Elsevier, 2003.